J. Fluid Mech. (2008), *vol.* 609, *pp.* 87–110. © 2008 Cambridge University Press
doi:10.1017/S0022112008002413 Printed in the United Kingdom

The viscous catenary revisited: experiments and theory

JOHN P. KOULAKIS[1], CATALIN D. MITESCU[1],
FRANÇOISE BROCHARD-WYART[2],
PIERRE-GILLES DE GENNES† AND ETIENNE GUYON[3]

[1]Department of Physics, Pomona College, 610 N. College Ave., Claremont CA 91711, USA

[2]Laboratoire PCC Institut Curie/CNRS UMR 168, 11 rue P. & M. Curie, 75231 Paris Cedex 05

[3]École Supérieure de Physique et de Chimie Industrielles, Laboratoire PMMH/CNRS UMR 7636,
10 rue Vauquelin, 75231 Paris Cedex 05

(Received 31 August 2007 and in revised form 9 May 2008)

Detailed observations have been performed on the evolution of a viscous catenary, a rope of high-viscosity fluid suspended from two points falling under gravity. Stroboscopic imaging techniques are used to obtain the position and shape of the strand as a function of time. Depending on their initial thickness and profile, the filaments are observed to evolve into either a quasi-catenary, or other, more complex shapes. A conceptually simple, energy-based theory is developed and compared with observations. It is shown to describe reasonably, except for a scaling in the time scale, the catenary-like regime.

1. Introduction

Viscosity is usually measured in terms of a resistance to shear; but it could also be evaluated by allowing a fluid filament to fall vertically and observing its shape and flow rate. This latter technique is used in particular to characterize the different regimes of sugar concentration in candy making (see Quintas *et al.* 2006; Rombauer, Becker & Becker 2006). In a Newtonian fluid, the elongational viscosity which resists stretching in a filament is simply given by $\eta^* = 3\eta$ (see Trouton 1906): the factor of 3 comes from the addition of the effect of the longitudinal velocity gradient (2η) and a pressure contribution required to ensure incompressibility as the jet is being elongated and squeezed. However, elongation is not used as often as shearing to measure viscosity because additional capillary effects, which resist stretching, also lead to jet instabilities. Possible viscoelastic effects in fast flows must also be considered; however, we will see that in our experiment these contributions are negligible.

The effect of elongational viscosity is somewhat similar to that of the resistance to strain in a solid wire, if we replace the relative strain by the strain rate (see Stokes 1845). Similar connections between elastic and viscous behaviour are obtained if a filament is bent or twisted. This amusing correspondence between a solid rope and a tube of viscous liquid leads to spectacular similarities: a honey filament falling vertically on top of a horizontal piece of bread coils on itself in a regular fashion just like a navy rope landing on a wharf. The coiling of a viscous filament has been analysed in

---

† Professor de Gennes died during the preparation of this paper.

several papers since the pioneering work of Barnes & Woodcock (1958) and Barnes & MacKenzie (1959), fifty years ago. In particular, Taylor (1968) realized that the basic mechanism was the result of the buckling instability caused by the compression of the tube. The problem was recently revisited by Mahadevan, Ryu & Samuel (1998, 2000), who demonstrated that the relative balance of viscous and inertial forces governed the phenomena of coiling, calculated a scaling law for the radius of the coil, and confirmed their results experimentally. The problem was re-examined in greater detail by Maleki *et al.* (2004) and Ribe (2004), who showed that there are additional regimes depending on the relative effects of not only viscosity and inertia, but also gravity.

In the analysis of these latter phenomena, relating to highly viscous liquids, capillary effects play a minor role. This is in contrast to the case of a jet of water where the Rayleigh–Plateau instability (Plateau 1873, 1881; Rayleigh 1892), resulting from the amplification of an initial deformation of a jet by means of the Laplace force, leads to its breaking up into a series of drops. On the time scale of our observations, ∼10–20 s, we do not observe significant capillary effects of the Rayleigh–Plateau type.

The present paper deals with a second situation studied theoretically by Teichman & Mahadevan (2003), in which a horizontal filament of viscous liquid (obtained by rapidly pulling apart a drop) is allowed to sag under its own weight. The problem resembles, at first glance, that of the classical catenary formed by a uniform chain held fixed at its two ends, hanging freely under gravity. That particular problem was first suggested two centuries ago by Jacob Bernoulli, and independently solved by Johann Bernoulli, Gottfried Leibniz, and Christiaan Huygens. However, the 'viscous catenary' is, of course, not in static equilibrium. In the experimental part of the present paper, we report observations carried out on the evolution of a viscous catenary. In fact, the deformation of a liquid is only qualitatively similar to the elastic problem; we observe experimentally (see figure 1) that several regimes are encountered depending on the initial geometry and thickness of the filament.

In § 3 of this paper, we present detailed and precise experimental observations of various regimes of the viscous catenary. In contrast, Teichman & Mahadevan (2003) include a limited set of experimental observations presented to illustrate the extensive theoretical analysis which makes up the bulk of their paper. They consider the entire solution by matching the central solution, where elongational effects are dominant, to that near the suspension points, where bending effects are important and dynamic boundary layers appear. In our experiments, the boundary layers are confined near the supports where we have no direct control, and elongational effects appear dominant over most of the filament. We also present some preliminary experimental results on the sagging of thinner filaments, where capillary effects become important and a different evolution is observed.

In § 4, we present a simplified theoretical analysis of the falling filament, based on energy considerations, which leads to simple calculations of the limiting cases. We further find that a variational calculation based on the same energy considerations shows reasonable agreement with experiments in the regime of moderately thick filaments. In § 5, we compare our simplified theory to the different regimes observed experimentally. In Appendix A, a semi-quantitative criterion is introduced which accounts for the crossover between the regimes of moderately thick and thin filaments.

2. Experiment

In our experiments, we have used silicone oil of 100 000 cSt kinematic viscosity (CLEARCO silicone 'O'-ring lubricant) coloured using a soluble powder (courtesy

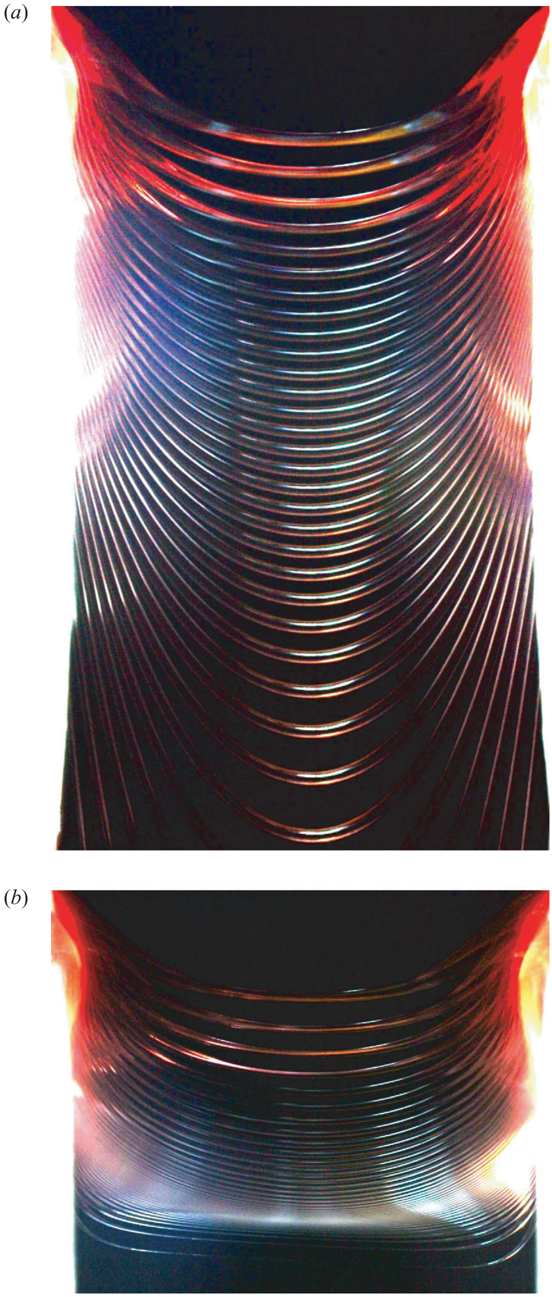

FIGURE 1. Stroboscopic images, taken at a strobe period of 0.420 s, illustrate the evolution of the two major and very different regimes of the falling liquid filaments. (*a*) A moderately thick filament of quasi-parabolic shape for which surface-tension effects appear negligible. (*b*) A thin filament, essentially assuming the form of a ‘U’, which appears to result from a combination of Laplace forces in the side sections and an extensive elongation of the middle region. In both images, the horizontal span is approximately 25 mm. For another set of images displaying both regimes, see Koulakis & Mitescu (2007).

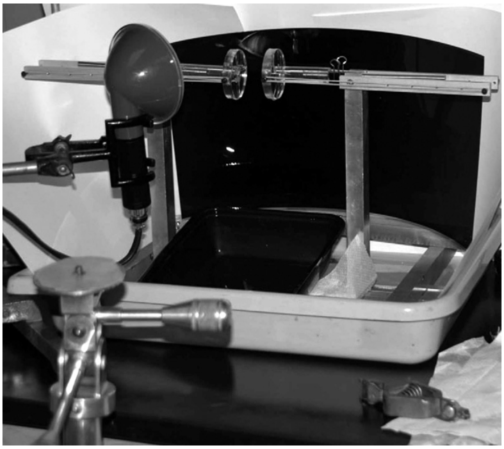

FIGURE 2. Experimental set-up. The strobe light is visible in the foreground. A small amount of the viscous silicone oil is placed between the two vertical disks, which are rapidly pulled apart by rubber bands. A polarizing filter in the background, together with a crossed polarizer on the camera lens, is used to reduce unwanted reflections of the strobe light.

of Neil Ribe, Institut de Physique du Globe, Paris) to increase visibility. We have checked that viscoelastic effects are insignificant in our configuration; CLEARCO rheological data indicates that the viscosity is constant for shear rates of less than $30\,\mathrm{s}^{-1}$and we estimate the shear rates of our filaments to be about $1\,\mathrm{s}^{-1}$. The case of a falling viscoelastic filament is discussed by Roy, Mahadevan & Thiffeault (2006).

In order to produce initial horizontal filaments, we use the following set-up. A pair of horizontal tubes are initially in contact and a drop of oil of controlled volume is placed at the upper central part of the tubes (figure 2). The tubes are rapidly pulled apart by four rubber bands up to their final separation of $L_0 \approx 30\,\mathrm{mm}$ in a fraction of a second. A continuous filament of oil is thus produced. However, some of the oil inevitably remains attached to the vertical portion of the two walls. As a result, we cannot study experimentally the effect of the boundary condition which was theoretically considered in the initial analysis by Teichman & Mahadevan (2003). As in the problem of the bending of a beam, it would be of interest to be able to consider the equivalent of singly supported (pinned), or clamped boundary conditions using an approximate geometry.

The evolution of the filaments such as those presented in figure 1 are obtained using a strobe light with a period of 0.01–0.80 s, and a 10–20 s camera exposure (Canon EOS 10D or EOS 30D digital camera). The strobe flash time of $\sim 5\,\mu\mathrm{s}$ can be considered effectively instantaneous at the speed of the fall of the thread. In order to obtain better illumination and contrast, we use crossed polarized filters on the camera and over the background, to suppress back reflection. The images were treated using Adobe Photoshop® and further analysed with the program GraphClick which detects changes of illumination. This has allowed us to determine with some precision the boundaries of the liquid strand as it is sagging.

Tiny bubbles or impurities and heterogeneities of the dye at random positions in the filament provide us with markers within the liquid. They indicate the path of an infinitesimal volume of liquid and can be used to determine the trajectory of specific points in the filament. By integration within the boundaries of the filament between corresponding markers, we have been able to verify, within an experimental accuracy of $\sim$5 %, the conservation of fluid (for further details see Koulakis (2006) § 5.2 pp. 40–41.). This shows indeed that there is no longitudinal flow of fluid along the filament, other than that due to stretching, as assumed in the theoretical treatment.

3. Observations

Different experimental behaviours are observed depending on the initial thickness and geometry of the filament. These behaviours represent various balances of gravitational effects, viscous resistance and surface-tension effects.

All filaments start in a straight horizontal position, supported at the two sides. For particularly thick filaments (with initial diameters greater than about 6 mm for strands approximately 60 mm long), the evolution is similar to a free-falling object barely hanging from two side filaments. The central section remains almost horizontal over most of its length while it essentially drops. Adhesion to the walls creates two increasingly thin strands that connect to the much thicker central cylindrical section and cause it to have some slight upward curvature. In this case, gravitational effects are balanced by the increase in kinetic energy of the main portion of the filament. Viscous dissipation in the two, thin, side filaments accounts for only a small fraction of the change in gravitational potential energy.

At the other extreme, for exceedingly thin filaments (less than about 0.1 mm for a strand approximately 20 mm long), the filament is formed and breaks in the middle almost immediately, after falling very little if at all. It appears that, in this case, surface-tension forces dominate and lead to rupture. For such diameters, the rise time of the Rayleigh instability is typically less than 1 s (Rayleigh 1892; Brochard-Wyart & de Gennes 2007).

The more interesting cases arise for moderately thick to thin filaments. In such cases, the initial behaviour is similar. The filament begins to drop or sag from the middle at an accelerating pace, forming an almost circular arc that becomes deeper and longer as it falls. The stretching during this phase occurs predominantly in the central region. When the lowest point has fallen approximately a tenth of the unstretched length of the filament, it begins to slow down.

At this point, we must differentiate between moderately thick and thin filaments. In the former case, the effect of gravity is almost balanced by viscous resistance, but surface-tension effects remain negligible. The filament forms a quasi-parabolic shape and evolves as described in § 3.1. If the filament is sufficiently thin that surface-tension forces become comparable to viscous resistance and gravitational forces, its evolution is more complicated. It progresses from a circular arc, to a parabolic shape, to an almost completely stationary form, and eventually a deep ‘U’, as described in § 3.2. In Appendix A, due to Christophe Clanet, an explicit physical criterion is provided which helps to differentiate between these two regimes.

3.1. *Quasi-parabolic catenary*

When surface-tension effects are negligible, the filament maintains a quasi-parabolic shape, falling as in figure 1(*a*). We observe this behaviour in strands with an initial diameter around 0.6–2 mm and an initial length of approximately 30 mm. In figure 1(*a*), we display a stroboscopic multiple-exposure image at strobe intervals of 0.420 s. Throughout the evolution, the diameter of the filament is considerably larger near the supports than throughout the rest of the filament. The diameter is observed to be almost uniform along most of the length, over the range of times when the filament is falling the slowest.

After the initial slowdown as detailed above, the filament resumes a downward acceleration. The stretching no longer occurs predominantly in the middle, as it did initially, but rather in the regions between the supports and the middle. Consequently, the centre remains relatively thick while the sides strain to support it. The filament continues thinning at the sides until rupture, in accordance with the predictions of Teichman & Mahadevan (2003).

3.2. *'U' shaped filament*

When the filament is thin (with an initial diameter of about 0.2–0.4 mm and initial length of about 30 mm), the evolution takes a different course. After the initial deceleration, the filament continues to slow down and comes to an almost stationary 'U' shape, evolving very slowly (see figures 1*b*, 3 and 4*a*). This is in contrast to the quasi-parabolic evolution, which displays only a relative slowing.

While the filament approaches this 'stationary' phase, we believe that the dominant stress on the middle of the filament is a result of viscous resistance to the tendency of the sides to hang vertically. As a crude model, we can think of the sides as two hanging bars pivoting about their supports, connected by a thin strand of fluid. The fluid between them stretches as the bars swing to a vertical position. This model is fairly descriptive of what we, in fact, observe if we recognize that the side 'bars' are actually fluid, curved and do display some change of shape (figure 3). As the filament becomes 'stationary' the central region flattens out. At the same time, the sides become more and more vertical, pulling on the middle and contributing to the straightening effect.

While the initial deceleration was a result of viscous resistance, we believe there is an additional mechanism at work that brings it to an almost complete stop. We observe that the thicker regions of the filament nearer the supports – the hanging 'bars' described in the preceding paragraph – contract, as would be expected from surface-tension effects. In figure 4(*b*), we see that if we look at the side regions, the paths travelled by tiny particles in the oil have a slight negative slope near the support. Even though the printing of the figure renders this somewhat difficult to see, a closer analysis reveals that the particles move upwards as they move towards the side, meaning that the filament is contracting in these side regions.

In other words, while the filament appears visibly stationary, it must be dynamic. The centre region prevents the two sides from falling to a completely vertical position, and in doing so, must stretch. In effect, the horizontal tension acts on the non-uniform filament – which is thicker at the ends and thinner at the centre – thus causing the thin bit in between to be pulled apart while the thicker sides do not fall very far, or even contract. As can be seen from the curves in figure 4(*d*), which represent the positions of small bubbles or particles in the filament, almost all the stretching occurs from an initially small central region. The additional length created from the elongation in the central region is partially offset by the contraction of the sides, thus giving the illusion of a 'stationary' shape.

When the rate of elongation in the central region is comparable to the rate of contraction in the side region, the filament appears temporarily stationary while thinning. However, as the filament becomes thinner, it stretches faster. A point is reached where the rate of elongation is greater than that of contraction, and the centre region of the filament is observed to fall again because the sides are now approaching verticality. As a result of this, the entire flat central region resumes a downward acceleration until ultimate rupture in the middle. This is again in contrast to the quasi-parabolic evolution, which ruptures on the sides.

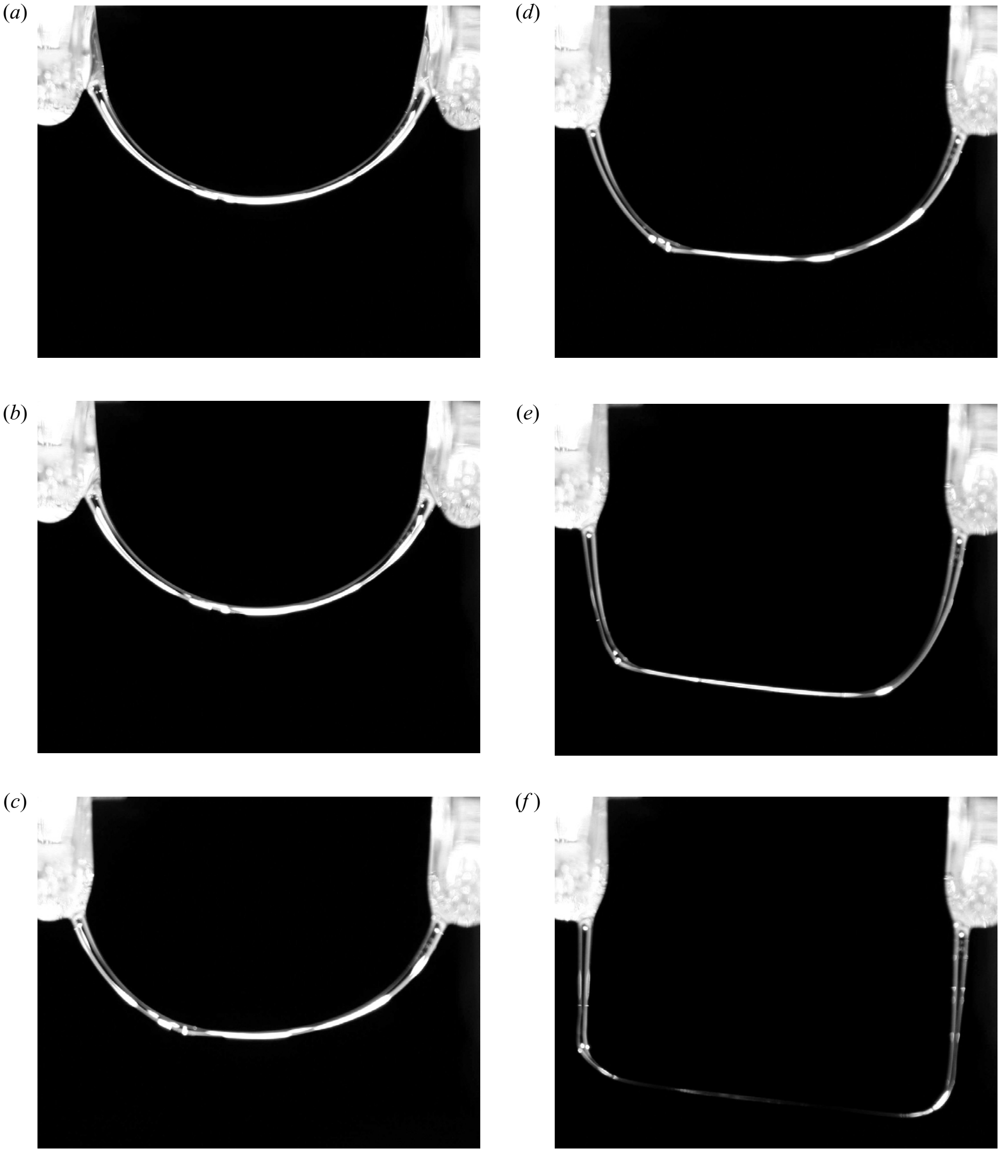

FIGURE 3. The mechanism of the 'U' formation. The sequence is taken at unevenly spaced time intervals. The sides pull on the middle as they progress towards a completely vertical hanging position, forming a straight thin central segment.

A special case of this type of evolution is shown in figure 5. Two points are visible that seem to remain temporarily stationary as the filament bends and straightens about them. The fluid between them moves upwards as the sides lower until the strand between them is almost completely horizontal. This behaviour may be a result of the balance between the rate of contraction and the rate of elongation.

3.2.1. *The central region of a 'U'*

We have found that the curves visible in figure 4(*d*) can be reproduced by a simple model. The strain rate of a Newtonian fluid is linearly proportional to the stress

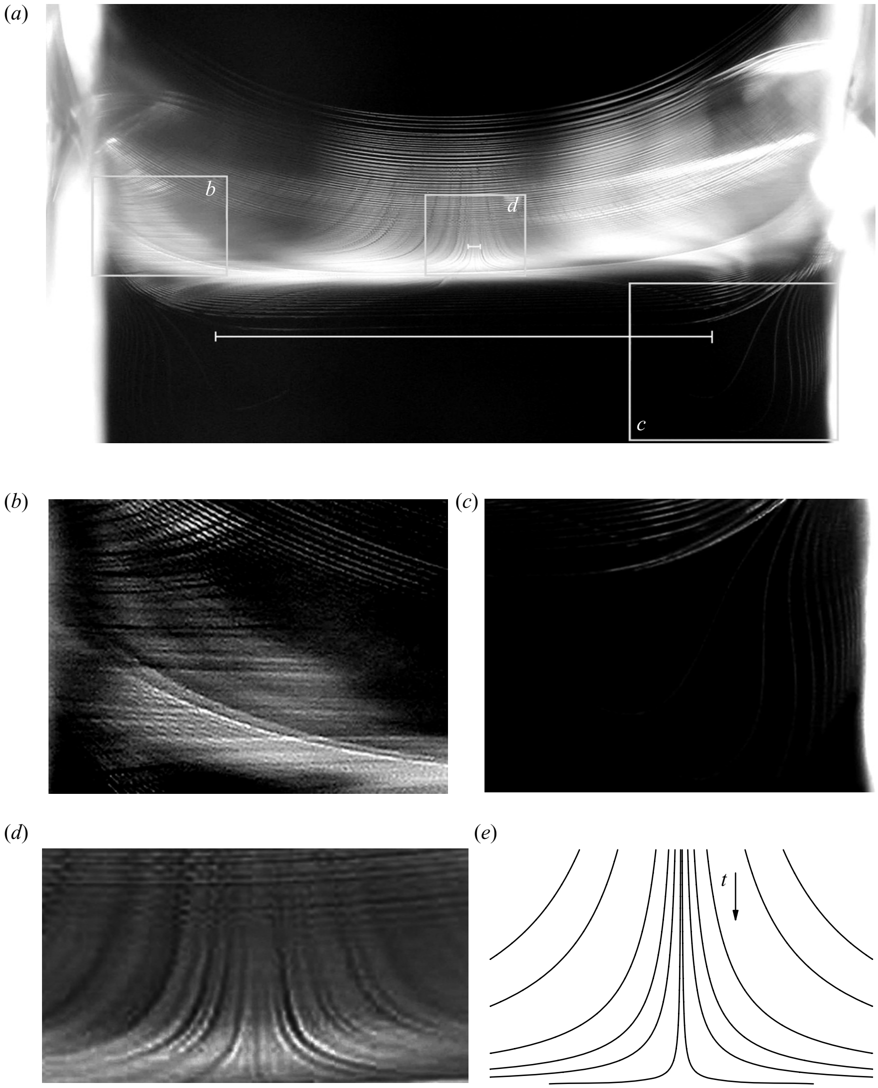

FIGURE 4. (*a*) Full view of the evolution of a ‘U’ shaped filament, strobe period 0.047 s. (*b*) Side region, discussed in § 3.2. (*c*) After rupture, discussed in § 3.2.3. (*d*) Centre region. (*e*) Family of curves predicted by (3.2). (*b*)–(*d*), correspond to the insets in (*a*). A small central piece, outlined below the middle of inset *d* in (*a*), about 0.3 mm long, stretches to approximately 12 mm just before rupture (indicated by the long white overlay line in (*a*)). The entire filament, initially 20 mm long, measures only 26 mm at rupture. The sides must be contracting, since the tiny central segment grows by nearly 12 mm while the total length increases by only about 6 mm. The theoretical curves of (*e*), discussed in § 3.2.1, are to be compared with (*d*).

applied. If we assume that the longitudinal tension F_T in the flat central region of uniform cross-sectional area A, is approximately constant (we recognize that this assumption is only a first-order approximation but, for the purposes of this derivation, it is only significant that the tension vary by much less than an order of magnitude), an element of fluid of length L must obey,

$$\frac{F_T}{A} = C\frac{\dot{L}}{L}, \tag{3.1}$$

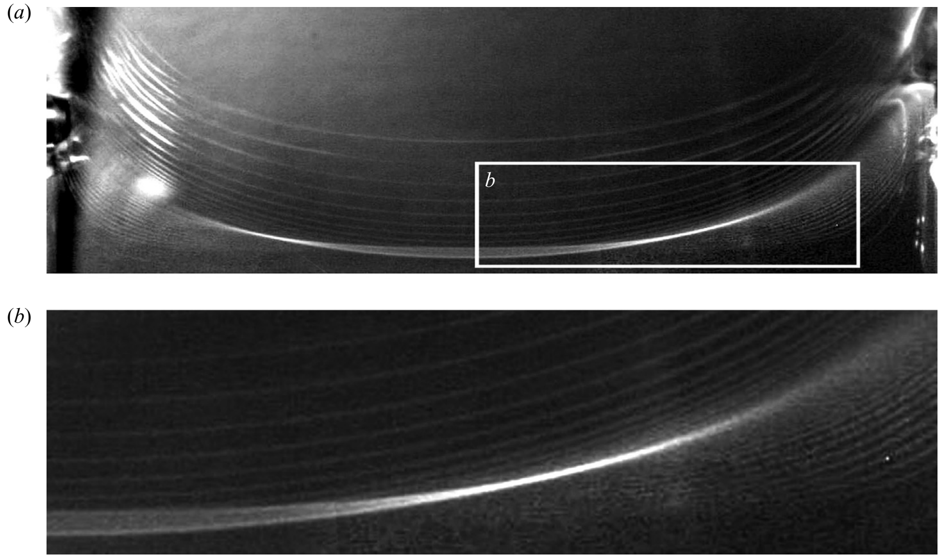

FIGURE 5. (*a*) In this special case of ‘U’-type evolution (observed with strobe period 0.25 s), the central region of the filament moves upwards after its initial descent. Two symmetric points are formed that appear to be stationary, of which one is shown in enlarged form in (*b*). As the central region becomes flatter, the filament seems to bend about these points, moving up in the space between them and down on the sides.

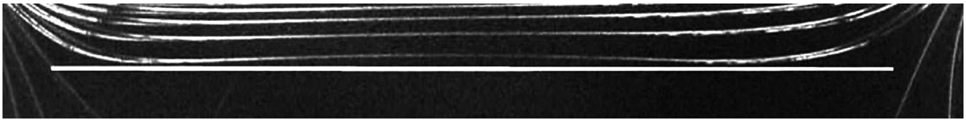

FIGURE 6. An example of a thin strand that evolves similarly to figure 4 producing a ‘w’ shape just before rupture. The white, horizontal line is superimposed on the image to emphasize the downward curvature in the centre. As seen in figure 7, the ‘w’ shape becomes very much more pronounced after rupture. (The strobe period here is 0.047 s and the supports are approximately 20 mm apart.)

where C is a constant. To conserve volume, $A = A_1 L_1 / L$, where A_1 is the original cross-sectional area corresponding to an initial length L_1. This implies,

$$\frac{F_T}{A_1 L_1 C} = \frac{\dot{L}}{L^2} \quad \rightarrow \quad (t - t_0) = \frac{A_1 C}{F_T} \frac{(L - L_1)}{L}. \tag{3.2}$$

Various values of L_1 produce the family of solution curves of (3.2), and its reflection about the vertical axis, displayed in figure 4(*e*), with $F_T/(A_1 C) = 0.001$, an arbitrary value; t is increasing downwards. The resulting curves strongly resemble the paths travelled by the tiny bubbles or particles in figure 4(*d*).

3.2.2. *‘W’ shape*

We have also observed that on the thinnest strands, in the moments just before rupture, the middle of the filament falls more slowly than the sides supporting it, creating a region with downward concavity vaguely resembling a ‘w’ (figure 6). This effect may be due to air drag, as the filament is very thin. Treating the centre of the filament as an infinite cylinder falling through a viscous medium (air), the drag per

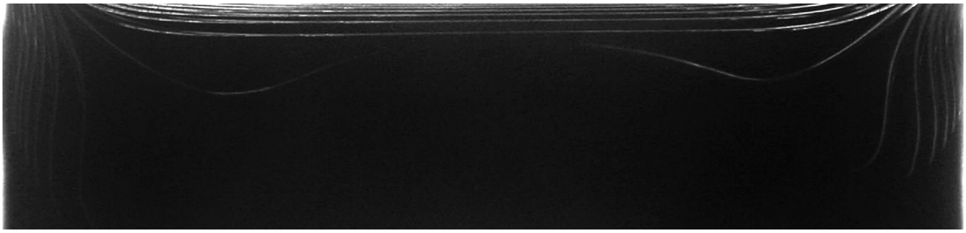

FIGURE 7. A strand that evolves similarly to those in figures 3, 4 and 6 producing a very pronounced 'w' shape after rupture, observed with a strobe period of 0.074 s. The first strand showing a clear 'w' shape is the one immediatly after rupture. Larger air drag in the central region slows down the tip's fall, creating the interesting profile. As the strands reach their vertical hanging position, they contract as a result of the Laplace force. A possible additional contribution could come from whiplash effects similar to a snapping string.

unit length is given approximately by Batchelor (1967, pp. 245–246),

$$F_D = \frac{4\pi\eta U}{\log(7.4/Re)}, \tag{3.3}$$

where U is the velocity of the fluid around the cylinder and Re is the Reynolds number. Plugging in our measured values, $U \approx 4.6\,\mathrm{mm\,s^{-1}}$ and $Re \approx 0.01$ yields a value of $F_D \approx 30\,\%$ of the weight per unit length at the centre of the horizontal segment. This value drops to $F_D \approx 15\,\%$ for the much thicker sides of the horizontal segment. This difference in the effect of air drag may be sufficient to produce the 'w' shape.

In addition, there may be a further effect due to the reduction of drag when the motion of the filament has a component parallel to its length, similar to the case of a cylindrical rod falling at an angle through a viscous fluid, which moves obliquely relative to its inclination (for further discussion see Guyon *et al.* 2001).

3.2.3. *After rupture*

In 'U'-type evolution, rupture occurs in the middle of the filament (figure 7). This very clear and pronounced 'w' shape, although broken in the middle, is almost always observed after rupture, whether or not the 'w' was noticeable before the break. We believe that this pronounced 'w' is a result of whiplash forces, similar to those observed when a string snaps. The subsequent motion of the two halves of the filament is similar to that of a freely falling chain tip, considered by Tomaszewski, Pieranski & Geminard (2006). The part of the free-falling filament that was nearest to the break falls more slowly than the region next to it. As a result, the free tip evolves from an initially downward curvature immediately after rupture, to an upward curvature as it falls. It forms a shape similar to an upward-facing hook that straightens as it falls to a completely vertical position (see figure 4*c*). The Laplace force continues to pull the fluid up, resulting in a contraction of the filament as it approaches its final hanging position.

This situation was considered in an independent experiment where oil coating a pointed rod is allowed to drop vertically from its tip. A drop formed on the tip of the rod falls, stretching a thin filament behind it and eventually breaking off. The remaining filament starts moving up vertically with dynamics governed by surface tension and elongational viscosity (Zylstra 2007), as will be reported elsewhere.

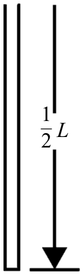

FIGURE 8. The model for very long deformations. Here, the filament is assumed to consist of two long thin parallel strands effectively joined together at the bottom by a horizontal segment of negligible length.

4. Theory

A thorough but complex mathematical analysis was carried out by Teichman & Mahadevan (2003). We will first outline below the simpler formulation developed by Brochard-Wyart & de Gennes (2007) which reproduces the early-time results of Teichman & Mahadevan (2003). However, we also include an inertial term, omitted by both sets of the cited authors, which renders the physics in the limiting cases quite different and provides better agreement with the experimental early-time behaviour.

For a filament falling under gravity, the rate of energy gained from the decrease in potential must be equal to that of energy dissipated in the fluid by stretching, plus that of its translational kinetic energy. This dissipation from stretching is given by

$$T\dot{S} = \tfrac{1}{2}\Omega\eta\dot{\epsilon}^2 = \tfrac{1}{2}M\nu\dot{\epsilon}^2, \tag{4.1}$$

where T is the temperature, and S is the entropy, so that the quantity $T\dot{S}$ is the change in energy per unit time; $\Omega = M/\rho$ is the volume of the filament, where M is the mass, ρ is the density; $\dot{\epsilon}$ is the strain rate, $\eta = \rho\nu$, the dynamic viscosity, and ν, the kinematic viscosity. We recognize that $\eta\dot{\epsilon}$ is the viscous stress, which multiplied by the strain rate gives the dissipation per unit volume (for further discussion see Batchelor 1967, pp. 112–115). Since this system consists of one-dimensional elongational flow, the viscosity in (4.1), which resists stretching, should be obtained from the Trouton viscosity, η^*, so that $\nu^* = \eta^*/\rho = 3\nu$ (see Trouton 1906). This gives a simple understanding of the system that is useful in developing an intuition of the mechanics involved. However, this does not take into account the effects of surface tension nor any variation in the diameter of the filament.

For theoretical clarity, we analyse the limiting cases of large deformations and early-time behaviour, first. However, the bulk of our experimental data is related to the intermediate-range behaviour which we discuss at greater length in § 4.3.

4.1. *Large deformations*

In the long-deformation limit, we model the filament as two long uniform vertical segments connected by a very short horizontal segment (figure 8). Assuming uniform stretching, we write by inspection:

$$\dot{\epsilon} = \frac{\dot{L}}{L}, \quad \bar{y} = \frac{L}{4}, \tag{4.2a, b}$$

where L is total length of the filament (initially L_0), and $\bar{y}$ is the position of the centre of mass. Then the viscous dissipation equation, (4.1), becomes,

$$\tfrac{1}{2}\Omega\eta\dot{\epsilon}^2 = \frac{M\nu^*}{2}\left(\frac{\dot{L}}{L}\right)^2. \tag{4.3}$$

The maximum vertical velocity is $\dot{L}/2$, so the vertical velocity v at any height y is,

$$v = \frac{\dot{L}}{L}y \quad \text{for} \quad 0 \leqslant y \leqslant \frac{L}{2}. \tag{4.4}$$

Then the kinetic energy is given by,

$$K = \tfrac{1}{2}M\int_0^{L/2}\left(\frac{\dot{L}}{L}y\right)^2\frac{\mathrm{d}y}{L/2} = M\frac{\dot{L}^2}{24}, \tag{4.5}$$

and by energy balance we have:

$$\frac{\mathrm{d}}{\mathrm{d}t}\left(\frac{gL}{4} - \frac{\dot{L}^2}{24}\right) = \tfrac{1}{2}\nu^*\left(\frac{\dot{L}}{L}\right)^2 \quad \rightarrow \quad 1 - \frac{\ddot{L}}{3g} = \frac{2\nu^*}{g}\frac{\dot{L}}{L^2}. \tag{4.6}$$

As we must eventually work out numerical solutions, we now introduce a scaled dimensionless time $\tau = t/t_g$, where $t_g = \nu^*/(9gL_0)$†, and a scaled length $\ell = L/L_0$ in terms of which (4.6) can be re-written as:

$$1 - \frac{27gL_0^3}{\nu^{*2}}\frac{\mathrm{d}^2\ell}{\mathrm{d}\tau^2} = \frac{18}{\ell^2}\frac{\mathrm{d}\ell}{\mathrm{d}\tau}. \tag{4.7}$$

(Note that the inertial terms in (4.7), (4.18) and (B 12) are scaled by a quasi-Reynolds number $Re^* = gL_0^3/\nu^{*2} = (L_0^2/\nu^*)/(\nu^*/(gL_0)) \sim t_{diffusion}/t_g$. This was independently pointed out by Ribe, personal communication (2006).)

We insert the values $\nu^* = 0.3\,\mathrm{m^2\,s^{-1}}$, $g = 9.81\,\mathrm{m\,s^{-2}}$, and $L_0 = 0.030\,\mathrm{m}$ to obtain,

$$1 - 0.0794\frac{\mathrm{d}^2\ell}{\mathrm{d}\tau^2} = \frac{18}{\ell^2}\frac{\mathrm{d}\ell}{\mathrm{d}\tau}. \tag{4.8}$$

Omission of the second-derivative term, coming from the kinetic energy contribution, leads to a simple analytic solution. Selecting an arbitrary value $\ell = 3$, for $\tau = \tau_0$ the solution is,

$$\ell = \frac{18}{6 - (\tau - \tau_0)}. \tag{4.9}$$

This leads to the prediction of Brochard-Wyart & de Gennes (2007), that the length diverges at a finite time $(\tau - \tau_0) = 6$, a seemingly unphysical result which implies accelerations larger than gravitational in the region just prior to the divergence. We here recognize that this divergence arises as a mathematical artefact resulting from forcing energy that would be accounted for by kinetic energy to be dissipated by viscous stretching instead. As ℓ approaches infinity, $\mathrm{d}\ell/\mathrm{d}\tau$ must also diverge to keep the product $(1/\ell^2)/(\mathrm{d}\ell/\mathrm{d}\tau)$ constant. Inclusion of the kinetic energy term in (4.8) leads to the numerical solutions shown in figure 9, which no longer display any such divergence.

Because of the conservation of volume, it is clear that the filament in this limit will become extremely thin. At this point, Rayleigh–Plateau effects cannot be ignored

---

† In defining $t_g = \nu^*/(9gL_0) = \nu/(3gL_0)$, we have chosen the numerical constant such that (4.20) assumes a particularly elegant form. Thus, our characteristic scaling time differs by a factor of two from that given in Teichman & Mahadevan (2003) and Brochard-Wyart & de Gennes (2007).

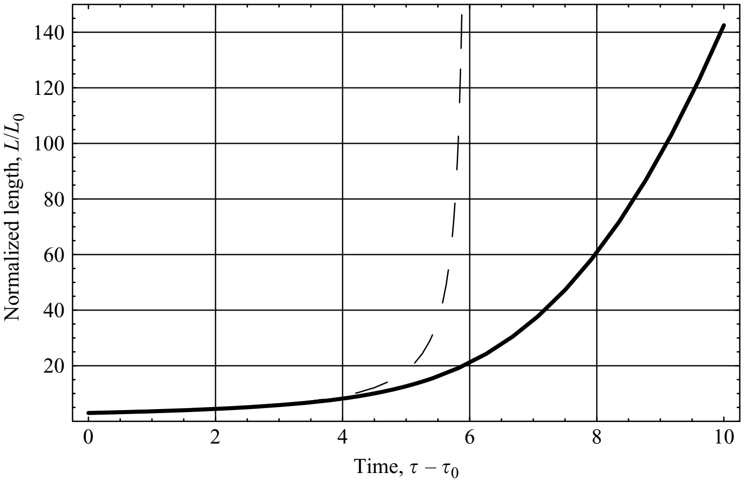

FIGURE 9. Long-term behaviour as predicted by simple approximations. The inclusion of the kinetic energy term (solid line) (4.7) eliminates the divergence of the length at finite times, as otherwise predicted by Brochard-Wyart & de Gennes (2007) (dashed line) (4.9).

(Brochard-Wyart & de Gennes 2007). These should be compared with pinch-off effects discussed in detail by Teichman & Mahadevan (2003) to determine which mechanism will lead to ultimate rupture. As this limit is far beyond the range of our experimental observations, we will not elaborate on this further.

4.2. *Small deflections*

In their full solution, Teichman & Mahadevan (2003) include the effects of bending at the boundaries, deriving a dependence of the maximum deflection, linear in time, for times less than $t_c = 32\nu r^3/(\pi g L_0^4)$, where r is the radius of the filament. For our experimental parameters, $t_c < 10^{-4}\,s$, unobservable in our experiments. Beyond this time, Teichman & Mahadevan (2003) show that elongation effects dominate. Brochard-Wyart & de Gennes (2007) discuss only this stretching regime. We will follow their formulation, but include an inertial term absent from both previously cited works.

For small deformations, we approximate the filament as being an arc of a large circle (figure 10). Let R be the radius of the circle, $2\theta_m$ be the angle spanned by the filament, and y_m be the distance the middle of the filament has fallen. Then,

$$y(\theta) = R(\cos\theta - \cos\theta_m) \approx \frac{L_0\theta_m}{4}\left(1 - \frac{\theta^2}{\theta_m^2}\right). \tag{4.10}$$

For small deformations, the strain is,

$$\frac{L - L_0}{L_0} = 1 - \frac{\sin\theta_m}{\theta_m} \approx \frac{{\theta_m}^2}{6}, \tag{4.11}$$

which implies a strain rate of,

$$\dot{\epsilon} \approx \tfrac{1}{3}\theta_m\dot{\theta}_m. \tag{4.12}$$

Assuming a uniform cross-section, the position of the centre of mass of the filament relative to the initial position of the midpoint is given by,

$$\bar{y} = \tfrac{1}{2}L_0\left(\cot\theta_m - \frac{1}{\theta_m}\right) \approx -\tfrac{1}{3}R{\theta_m}^2 = -\tfrac{2}{3}y_m. \tag{4.13}$$

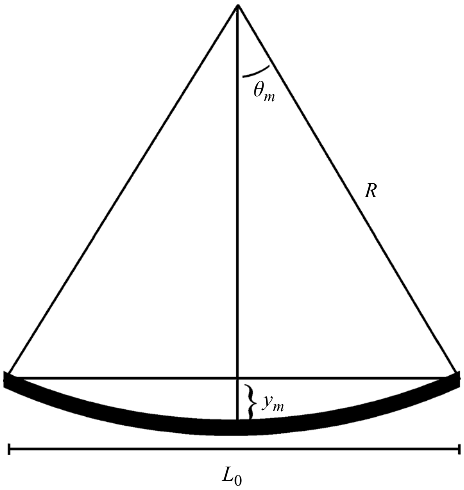

FIGURE 10. The model for small deformations. The filament is represented as a uniform arc of a large circle, of chord length L_0, spanning an angle $2\theta_m$.

Therefore, when written in terms of θ_m, the potential energy is,

$$-\tfrac{2}{3}y_m Mg \approx -\tfrac{1}{6}L_0\theta_m Mg. \tag{4.14}$$

The vertical velocity of a point on the filament is given by,

$$v_y = \frac{\mathrm{d}}{\mathrm{d}t}y(\theta) = \frac{L_0}{4}\left(1+\frac{\theta^2}{\theta_m^2}\right)\dot{\theta}_m. \tag{4.15}$$

Assuming the horizontal component of the velocity is small compared to the vertical component, the kinetic energy is,

$$K \approx \tfrac{1}{2}M\int_0^{\theta_m} v_y^2\frac{\mathrm{d}\theta}{\theta_m} = \frac{7ML_0{}^2}{120}\dot{\theta}_m^2. \tag{4.16}$$

Substituting the above results into the energy balance equation yields,

$$\nu^*\frac{\theta_m{}^2\dot{\theta}_m}{3} = L_0 g - \frac{7L_0{}^2}{10}\ddot{\theta}_m. \tag{4.17}$$

In terms of the dimensionless time, (4.17) can be expressed as:

$$\left(1-\frac{567gL_0^3}{10\nu^{*2}}\frac{\mathrm{d}^2\theta_m}{\mathrm{d}\tau^2}\right) = 3\theta_m{}^2\frac{\mathrm{d}\theta_m}{\mathrm{d}\tau}, \tag{4.18}$$

and, inserting the corresponding numerical values,

$$\left(1-0.1668\frac{\mathrm{d}^2\theta_m}{\mathrm{d}\tau^2}\right) = 3\theta_m{}^2\frac{\mathrm{d}\theta_m}{\mathrm{d}\tau}. \tag{4.19}$$

We note that if we drop the second-derivative term, which results from the inclusion of kinetic energy, the analytic solution for small values of time of Teichman & Mahadevan (2003) as well as that of Brochard-Wyart & de Gennes (2007) is obtained,

$$\theta_m{}^3 = \tau, \quad \text{i.e.} \quad \theta_m = \tau^{1/3}. \tag{4.20}$$

A numerical solution, corresponding to the inclusion of the kinetic-energy term, with initial conditions $\theta_m(0)=0$ and $\theta_m{}'(0)=0$ is displayed together with that of (4.20)

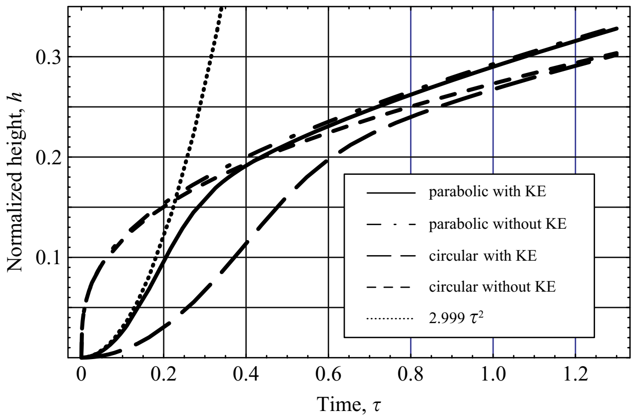

FIGURE 11. Start-up solutions as predicted by various models. Dropping the kinetic energy terms leads to the start-up solution $y_m \sim \tau^{1/3}$ as predicted by Teichman & Mahadevan (2003) and Brochard-Wyart & de Gennes (2007). We see this in the circular approximation (short dash line) (4.20) and with the parabolic approximation (dot-dash line) Koulakis (2006) equation 3.24. Including the kinetic energy terms yields (long dash line) (4.18) for the circular approximation or the (solid) curve (B 12) for the parabolic approximation. The (small dot) curve $y_m \sim \tau^2$ (4.21) corresponds to complete neglect of the viscous dissipation terms. Our experimental observations will be compared to the (solid) curve displaying the parabolic approximation with the inertial term.

in figure 11. It is evident that for small values of time, the right-hand side of (4.19) approaches zero, leading to a simple start-up solution,

$$\theta_m(\tau) = 2.997\tau^2. \tag{4.21}$$

To summarize, there are three different regimes for small times. A first regime, dominated by bending effects, is linear in time for extremely short times, unobservable in our experiment. A second region, where inertial effects are significant, leads to a quadratic time-dependence, which merges with the approximate $t^{1/3}$-dependence expected in the absence of inertia. As we elaborate below in § 5, our experimental evidence bears out the need for the inertial correction (see also figure 14).

4.3. *Parabolic approximation*

To account for the behaviour in the intermediate regimes, we assume that the shape is approximated by a parabolic function of the form,

$$y = -y_m\left(1 - \frac{4x^2}{{L_0}^2}\right) = -L_0 h\left(1 - \frac{4x^2}{{L_0}^2}\right), \tag{4.22}$$

where $h = y_m/L_0$ is a dimensionless measure of the height. This function is always equal to zero at $x = \pm L_0/2$ and has height y_m. Again, the change in potential energy must be equal to the change in kinetic energy plus the viscous dissipation. As the detailed mathematical solution of this system is tedious, we have included it as Appendix B.

5. Comparison with observations

Our experimental points (t_{exp}, h_{exp}) provide data only for time intervals with respect to an indeterminate start time and initial position, t_0 and y_0, respectively. We determine y_0 by estimating the initial position from our pictures, with an uncertainty

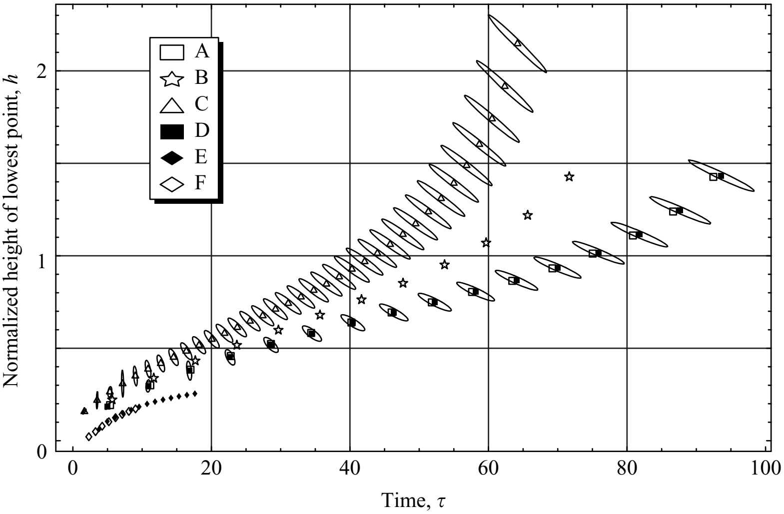

FIGURE 12. Measured values for the distance the lowest point of the filament has fallen. The ellipses represent our uncertainties, and have been removed from some data sets for clarity. Sets A, B, C and D are from quasi-parabolic runs whereas sets E and F are early points from filaments that eventually form a 'U'.

of ∼0.25 mm. We convert the y data points to the dimensionless height h, by dividing them by the initial length L_0. Because of the initial profile of the filament, which is not uniform as our theory assumes, but much thicker near the supports than in the middle, L_0 is not precisely defined from the pictures and there is some ambiguity as to its exact value. Consequently, this is our largest source of uncertainty, which is ∼2 mm for a strand ∼28 mm long.

To determine t_0, we first invert the theoretical function $h(\tau)$ as determined by the parabolic approximation, and express it as $\tau(h_{exp})$. If our theory is accurate, a graph of $\tau(h_{exp})$ *vs.* t_{exp} should cross the origin and be linear with a theoretical slope of $1/t_g = (9gL_0)/\nu^*$ (we denote the actual slope by $1/t_{gexp}$). Using the early points from each data set, for which the parabolic approximation should be more accurate assuming a relatively constant cross-section, we plot $\tau(h_{exp})$ *vs.* t_{exp} and calculate t_0 from the x-intercept. We also define a new variable, $\alpha = t_{gexp}/t_g$ to measure the agreement of the theoretical time scale with the experimental time scale.

Figure 12 shows our raw data points for four typical quasi-parabolic runs (runs A, B, C and D) similar to that in figure 1(*a*), for which we expect reasonable agreement. In addition, figure 12 displays data points for the early, still quasi-parabolic, behaviour of two runs (E and F) that eventually form 'U's as illustrated in figures 1(*b*) and 4. The ellipses display our uncertainty, which is estimated by applying the procedure detailed above using extreme but still reasonable values of L_0 and y_0. Error bars have been removed from a few runs for clarity.

We observe, from table 1, that these values deviate significantly from absolute agreement ($\alpha = 1$). For the quasi-parabolic cases, we have α in the range 6–10, whereas for the beginning of the 'U'-shaped runs $\alpha \sim 25$. If we adjust the experimental time scale by $1/\alpha$ (figures 13 and 14), we see that our data points collapse onto the same theoretical curve. Furthermore, we notice a fair consistency in the value of α for the different runs displaying similar behaviour. In other words, except for an important

Run	A	B	C	D	E†	F†
α	9.8 ± 1.6	8.2 ± 0.8	6.1 ± 1.0	9.9 ± 1.1	25 ± 5	24.4 ± 3.3
L_0 (mm)	28 ± 2.4	29 ± 1.6	21.5 ± 1.5	29 ± 1.6	29.5 ± 2	24.5 ± 2
Initial diameter (mm)	0.75	0.79	0.6	0.98	0.18	0.28

† Data sets E and F are points extracted from the early, still parabolic, behaviour of filaments that eventually form a 'U' shape. They display different behaviour from sets A, B, C and D, which remain in a quasi-parabolic shape throughout their evolution.

TABLE 1. The value of α for various runs.

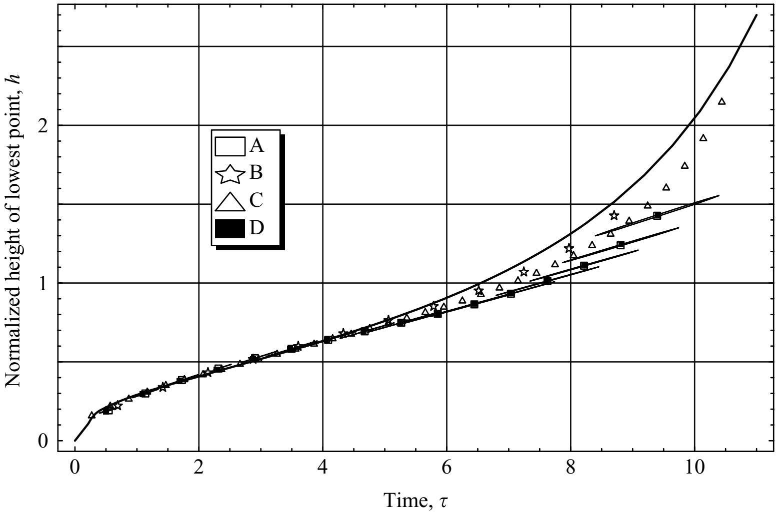

FIGURE 13. Adjusted observations and theory. The time scales of our data points have been adjusted by a factor of $\alpha \sim 9$, causing the points to collapse onto a single theoretical curve (B 12). The short lines appearing on data set D are the transformations of the corresponding uncertainty ellipses in figure 12.

adjustment in the time scale, the energy-based theory reproduces with moderate accuracy the behaviour of the filament.

The deviation from theory of the later points may be accounted for by the fact that our assumptions break down as time progresses. The parabolic approximation becomes inadequate and stretching is even less uniform.

The adjustment in the time scale must be explained either by having less energy available to dissipate than assumed or by having more energy dissipated for the same change in height. Since the filament is not initially of uniform radius, as assumed in our theoretical calculations, and there is more mass near the supports, less mass is falling, and therefore we have a smaller change in potential energy. In addition, the adhesion of fluid at the walls leads to bending in their immediate neighbourhood, further slowing the evolution. The net result is that the filament takes longer to fall through the same height.

A finite-difference calculation, illustrated in figure 15 (Ribe, personal comunication 2007), which includes surface-tension, gravity and viscous resistance to stretching and bending, appears to confirm our conjecture that a catenary with uniform cross-section

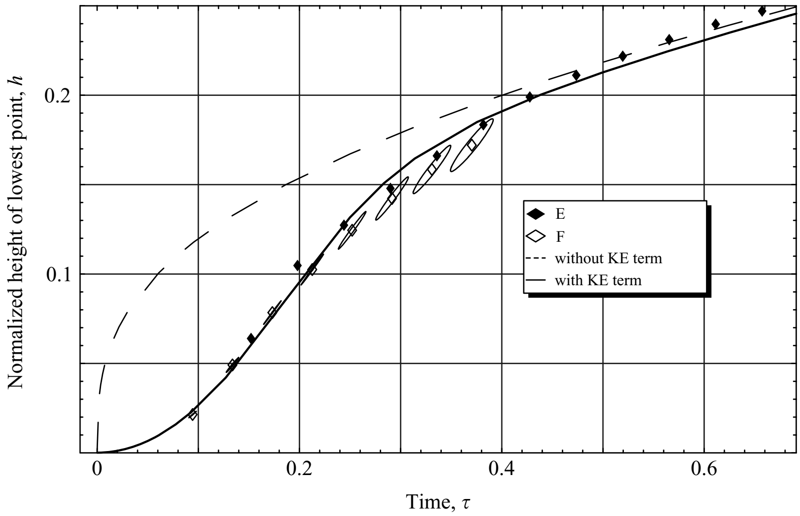

FIGURE 14. Adjusted observations and theory for the early behaviour. The time scales of our data points have been adjusted by a factor of $\alpha \sim 25$, again causing the points to collapse onto a single theoretical curve (B 12).

falls more rapidly than one with a similar central region, but widening cross-section near the walls. While Ribe's calculation shows that these effects are in the right direction, they are far from sufficient to explain the total discrepancy. However, we should also point out that his calculations involve only a difference of about a factor of four between the smaller radius of the filament at the centre and its value at the boundary walls. In our set of experiments, particularly those that show the largest numerical discrepancy in the time scale, this factor ranges between one and two orders of magnitude.

6. Conclusions

We note that the analysis of the behaviour of different filaments required the use of widely different factors in the time scales. The results displayed in figures 13 and 14, in which we see data from very different filaments collapsed onto a single curve, indicate an underlying universal scaling behaviour when an appropriate time-scale factor is used. This leads us to believe that the essential theoretical assumptions of our models are fundamentally correct and that the explanation for the differing time-scale factors must be more peripheral. Reasons for this may be related to the fact that the cross-sectional radii of the filaments are far from uniform, as assumed in the theory, and that the effects of surface tension, leading to contraction of the filament in the lateral regions, significantly complicate the evolution mechanism.

In the experiments reported in this paper, we have addressed the evolution of viscous filaments initially about 30 mm in length for a variety of initial diameters. For very thick strands (of diameter approximately 6 mm) the behaviour is uninteresting as the ends cannot support the total weight and the filament is almost in virtual free fall. For thinner filaments (of diameter approximately 0.6–2 mm) we have reproduced and precisely observed the regime initially described by Teichman & Mahadevan (2003) and have provided an alternative simplified theory which, particularly, includes an inertial term neglected by previous authors. This modified theory fits the data very reasonably, particularly in the early-evolution regime. For thin filaments (of diameter

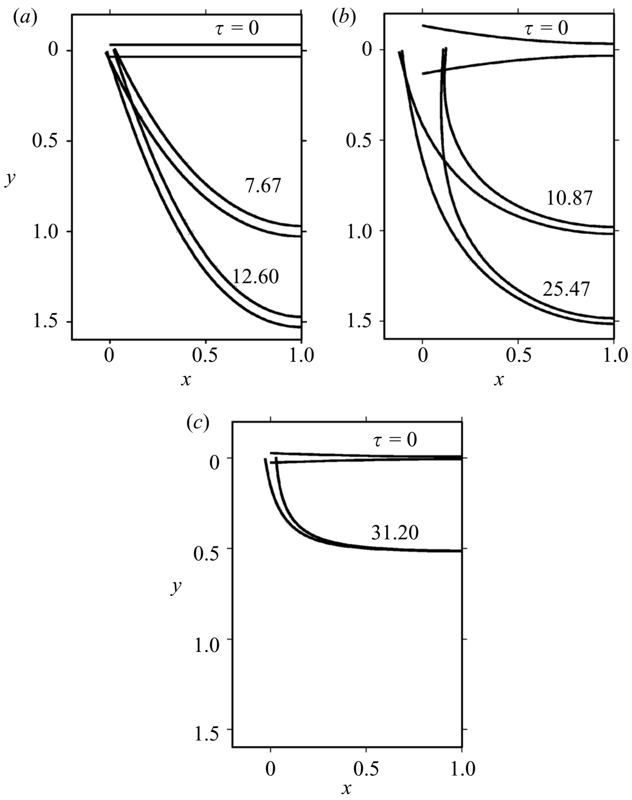

FIGURE 15. The evolution of three filaments, predicted numerically using the finite-difference method of Ribe (2003), modified to account for the filament geometry. The calculation includes the effects of surface tension, gravity and viscous resistance to stretching and bending, but neglects inertia. The parameters used were characteristic of our filaments, density $\rho = 971\,\mathrm{kg\,m^{-3}}$, surface tension $\gamma = 21.5 \times 10^{-3}\,\mathrm{N\,m^{-1}}$, and horizontal span $L_0 = 0.03\,\mathrm{m}$. The figures show only half of the strand and the axis labels are in units of $L_0/2$. The dimensionless time τ is expressed as t/t_g. The filament in (*a*) is initially of uniform radius, 0.5 mm. The filament in (*b*) has initially the same radius at the centre, but is tapered so that the radius at the wall (2 mm) is four times greater than that at the centre. Note that the time for the tapered strand to fall through a distance $y = 1$ is 1.4 times longer than for the uniform strand, and for $y = 1.5$ this time is twice as long, in accordance with our arguments in § 5. The filament in (*c*) is also tapered, but with a radius of 0.1 mm in the centre (and 0.4 mm at the wall). We see that this strand evolves into a 'U', confirming our arguments in § 3.2 and Appendix A, that the 'U' is a result of surface-tension effects; note also that the 'U' almost stalls around $y = 0.5$. For convenience of calculation, the boundary condition used was 'hinged' so that the filament is free to rotate about its centre point at the wall.

0.2–0.4 mm) we describe a 'U'-shaped evolution which has not been previously reported and for which we provide a semi-quantitative explanation. We have begun preliminary observations, not reported here, on the behaviour of filaments after the original system has broken. This behaviour, whether due to spontaneous breaking or to filaments deliberately cut by hot-wire or laser-beam techniques, appears to be an area of rich complexity which we propose to describe in detail in the future.

In parallel with the experimental work described in this paper, the theoretical part resulted, in early 2006, from discussions with P.-G. de Gennes and F. Brochard-Wyart, intended to revisit Mahadevan's original treatment by using the energy-based approach. As the present paper was being finalized, we experienced, in May 2007, the sad loss of our friend and collaborator Pierre-Gilles de Gennes. As a tribute to him, indicative of his approach to such problems, we decided to publish separately his initial calculations on this topic (Brochard-Wyart & de Gennes 2007). In the current paper, we have presented a brief review of his approach, and developed a more extended version based on our continued collaboration in the drafting stages of this paper.

We would like to acknowledge many illuminating discussions over the last two years with Neil Ribe and particularly thank him for providing the calculations and illustrations discussed in figure 15. We particularly thank Christophe Clanet for most useful recent discussions and for drafting the major part of the content of Appendix A. We are grateful to L. Mahadevan for a critical reading of an early version of the manuscript.

We thank the technical staff of the Pomona College Physics Department, especially Glenn Flohr and David Haley, for their support and gracious assistance through every stage of this project.

This work was originally supported by a grant from the Pomona College Summer Undergraduate Research Program to J. P. K. in the summer of 2005. A major portion of the work constituted J. P. K.'s undergraduate senior thesis presented in April 2006. The project was completed with support from a Pomona College Mellon Post-Baccalaureate Fellowship awarded to J. P. K. from February to July 2007.

Appendix A. Transition between the catenary and 'U' regimes

We are grateful to Christophe Clanet[†] for providing after recent discussions a draft of the following physical arguments for distinguishing the transition between the quasi-parabolic and 'U' regimes. His semi-quantitative arguments lead to an interesting new prediction, which we hope to verify in the future, that the distinction between the two regimes is independent of the viscosity and is based only on surface tension and geometrical parameters.

The experiments, described in this paper, conducted on horizontally hanging, viscous Newtonian-liquid threads, reveal that the initial cylindrical threads can undergo, as they bend under gravity, two types of deformation: either forming a quasi-parabolic shape (figure 1*a*) or a 'U' shape (figure 1*b*).

A physical argument is proposed to account for both shapes. The two regimes can be approximated by the following model involving an ideal massless thread on which a distribution of massive beads are attached. If the beads are equally spaced, the hanging thread exhibits a catenary-like shape (figure 16*a*). On the other hand, if the beads are concentrated close to the edges, the thread takes the form of two massive vertical parts connected by a very thin massless wire (figure 16*b*).

The physical argument proposed for the transition is thus as follows. If the liquid drains, by capillarity, towards the edges on a time scale shorter than the characteristic time of deformation, a 'U' shape will result. On the contrary, if the deformation takes place on a time scale short enough to preclude any drainage, the mass of the thread will remain relatively uniform and we will observe a quasi-parabolic shape.

As has been derived in § 4, the characteristic growth time for the deformation is $t_g = \nu^*/(9gL_0) \sim \eta/(\rho g L_0)$, which scales linearly with the viscosity and with the inverse of the thread length.

[†] Chargé de Recherche au CNRS, Professeur Chargé de Cours à l'Ecole Polytechnique, Laboratoire d'Hydrodynamique de l'Ecole Polytechnique (LadHyX), 91128, Palaiseau, France.

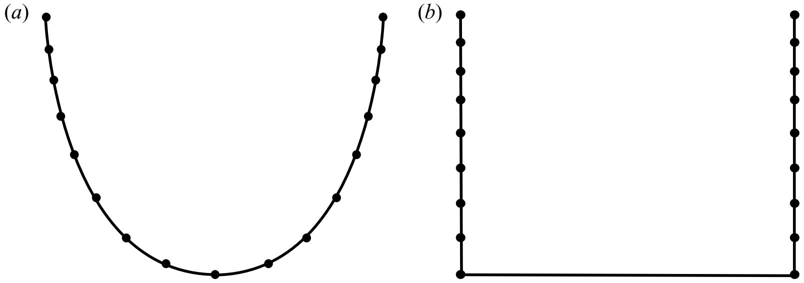

FIGURE 16. (*a*) Equally spaced massive beads on a massless string form approximately a catenary shape. (*b*) If the beads are concentrated along the edges, a squared ‘U’ shape forms.

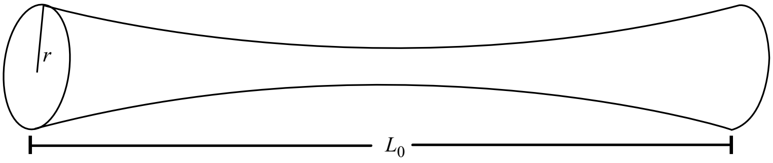

FIGURE 17. Conventions used to describe the drainage of the thread.

For the drainage time, we consider a horizontal thread, as in figure 17, evolving under surface-tension forces in the absence of gravity. In the Stokes regime, the capillary pressure gradient, γ/rL_0, balances the viscous dissipation, $\sim\eta V/L_0^2$, where r is the radius of the filament, γ is the surface tension, and V is the axial fluid velocity. This balance leads to a characteristic drainage time,

$$t_d \equiv \frac{L_0}{V} \sim \frac{\eta r}{\gamma}. \tag{A 1}$$

The crossover between the quasi-parabolic and the ‘U’ shapes can now be deduced from the ratio of the two time scales,

$$\frac{t_g}{t_d} \sim \frac{a^2}{L_0 r}, \quad a \equiv \sqrt{\frac{\gamma}{\rho g}}, \tag{A 2}$$

where a is the characteristic capillary length. According to this criterion, the transition for silicone oils ought to be independent of the viscosity and should depend only on the ratio between the surface a^2 and the surface of the thread rL_0 (because surface tension remains relatively constant for silicone oils of different viscosities). For small values of this ratio, the thread should deform without draining and the quasi-parabolic shape will be observed. On the contrary, with a very thin thread, this criterion predicts the formation of the ‘U’ shape. As we see in figure 3(*e*), where the drainage time is short, most of the fluid is drawn into the two side ‘arms’ observed in the figure, leaving a very thin, central region which continues to be stretched horizontally.

The inverse of the ratio in (A 2) appears in Brochard-Wyart & de Gennes (2007) equation 14, but they use this as a criterion to predict whether the filament will spontaneously rupture under Laplace forces before any elongation can be observed. If, however, we do not interpret this as a criterion for actual rupture, but for the incipient rupture, which leads to the formation of the thin, horizontal region of the ‘U’, this clarifies our earlier description (§ 3.2) of the mechanism of formation of the ‘U’.

Appendix B. Mathematics of the parabolic approximation

We assume that the filaments remains approximately in the shape of a parabola of the form,

$$y = -y_m\left(1 - \frac{4x^2}{{L_0}^2}\right) = -L_0 h\left(1 - \frac{4x^2}{{L_0}^2}\right), \tag{B 1}$$

where $h = y_m/L_0$ is a dimensionless measure of the height. This function is always equal to zero at $x = \pm L_0/2$ and has height y_m. The length of the filament is given by,

$$L = \int_{-L_0/2}^{L_0/2} \sqrt{1 + \left(\frac{\mathrm{d}y}{\mathrm{d}x}\right)^2}\,\mathrm{d}x = L_0 \int_0^1 \sqrt{1 + 16h^2u^2}\,\mathrm{d}u = L_0 F(h), \tag{B 2}$$

where we define $u = 2x/L_0$ and $F(h) = \int_0^1 \sqrt{1 + 16h^2u^2}\,\mathrm{d}u$. Taking the derivative of this with respect to time gives,

$$\dot{L} = L_0 \dot{h} \int_0^1 \frac{16hu^2}{\sqrt{1 + 16h^2u^2}}\,\mathrm{d}u = L_0 \dot{h} W(h), \tag{B 3}$$

where

$$W(h) = \partial F/\partial h = \int_0^1 \frac{16hu^2}{\sqrt{1 + 16h^2u^2}}\,\mathrm{d}u.$$

This implies a strain rate of

$$\dot{\epsilon} = \frac{\dot{L}}{L} = \frac{W(h)}{F(h)}\dot{h}. \tag{B 4}$$

The centre of mass of this parabola is given by,

$$\bar{y} = \frac{{L_0}^2 h\rho \displaystyle\int_0^1 (1 - u^2)\sqrt{1 + 16h^2u^2}\,\mathrm{d}u}{L_0\rho \displaystyle\int_0^1 \sqrt{1 + 16h^2u^2}\,\mathrm{d}u} = L_0 h \frac{P(h)}{F(h)}, \tag{B 5}$$

where $P(h) = \int_0^1 (1 - u^2)\sqrt{1 + 16h^2u^2}\,\mathrm{d}u$. Therefore, the time derivative of the centre of mass is given by,

$$\dot{\bar{y}} = L_0 \frac{FP + h(QF - WP)}{F^2}\dot{h}, \tag{B 6}$$

where

$$Q(h) = \partial P/\partial h = \int_0^1 \frac{16hu^2(1 - u^2)}{\sqrt{1 + 16h^2u^2}}\,\mathrm{d}u.$$

The vertical velocity of a point on the filament is given by,

$$v_y = \frac{\mathrm{d}y}{\mathrm{d}t} = -L_0(1 - u^2)\dot{h}, \tag{B 7}$$

and the amount of mass in a segment of length $\mathrm{d}L$ is,

$$\mathrm{d}m = M\frac{\mathrm{d}L}{L} = M\frac{\sqrt{1 + 16h^2u^2}}{2F(h)}\,\mathrm{d}u. \tag{B 8}$$

Assuming the horizontal velocity is negligible compared to the vertical velocity, the kinetic energy of the filament is given by,

$$K \approx \tfrac{1}{2}\int v_y^2\,\mathrm{d}m = \frac{M{L_0}^2}{2F(h)}\dot{h}^2\int_0^1 (1-u^2)^2\sqrt{1+16h^2u^2}\,\mathrm{d}u = \frac{M{L_0}^2}{2}\dot{h}^2\frac{R(h)}{F(h)}, \tag{B 9}$$

where $R(h) = \int_0^1 (1-u^2)^2\sqrt{1+16h^2u^2}\,\mathrm{d}u$. For simplicity, we also define,

$$S(h) = \frac{\partial R}{\partial h} = \int_0^1 \frac{16(1-u^2)^2u^2h}{\sqrt{1+16h^2u^2}}\,\mathrm{d}u. \tag{B 10}$$

Then, the change in K is,

$$\dot{K} = \frac{M{L_0}^2}{2}\left(2\dot{h}\ddot{h}\frac{R}{F} + \dot{h}^3\frac{SF-RW}{F^2}\right). \tag{B 11}$$

$F(h)$, $W(h)$, $P(h)$, $Q(h)$, $R(h)$ and $S(h)$ are all solved analytically by the use of Mathematica®.

From conservation of energy, we use (4.1), (B 4), (B 6) and (B 11) to arrive at,

$$FP+h(FQ-PW) = 81RF\frac{g{L_0}^3}{\nu^{*2}}\frac{\mathrm{d}^2h}{\mathrm{d}\tau^2} + \tfrac{81}{2}(SF-RW)\frac{g{L_0}^3}{\nu^{*2}}\left(\frac{\mathrm{d}h}{\mathrm{d}\tau}\right)^2 + \tfrac{9}{2}W^2\frac{\mathrm{d}h}{\mathrm{d}\tau}. \tag{B 12}$$

This equation is expressed in terms of our dimensionless time $\tau = t/t_g$, where $t_g = \nu^*/(9gL_0)$. We solve this equation numerically, in effect performing a variational calculation on the energy. The predictions of this model are displayed alongside our observations in figures 11, 13 and 14.

REFERENCES

Barnes, G. & Mackenzie, R. 1959 Height of fall versus frequency in liquid rope-coil effect. *Am. J. Phys.* **27**, 112–115.

Barnes, G. & Woodcock, R. 1958 Liquid rope-coil effect. *Am. J. Phys.* **26**, 205–209.

Batchelor, G. K. 1967 *An Introduction to Fluid Dynamics*. Cambridge University Press.

Brochard-Wyart, F. & de Gennes, P.-G. 2007 The viscous catenary: a poor man's approach. *Europhys. Lett.* **80**(3), 36001.

Guyon, E., Hulin, J.-P., Petit, L. & Mitescu, C. D. 2001 *Physical Hydrodynamics*, pp. 329–330. Oxford University Press.

Koulakis, J. P. 2006 The viscous catenary. Pomona College BA thesis available at http://ccdl.libraries.claremont.edu/cdm4/item_viewer.php?CISOROOT = /stc&CISOPTR = 3.

Koulakis, J. P. & Mitescu, C. D. 2007 The viscous catenary. *Phys. Fluids* **19**(9), 091103.

Mahadevan, L., Ryu, W. S. & Samuel, A. D. T. 1998 Fluid 'rope trick' investigated. *Nature* **392**, 140.

Mahadevan, L., Ryu, W. S. & Samuel, A. D. T. 2000 Correction: Fluid 'rope trick' investigated. *Nature* **403**, 502.

Maleki, M., Habibi, M., Golestanian, R., Ribe, N. M. & Bonn, D. 2004 Liquid rope coiling on a solid surface. *Phys. Rev. Lett.* **93**(21), 214502.

Plateau, J. 1873 *Statique des liquides soumis aux seules forces moléculaires*. Gauthier-Villars.

Plateau, J. 1881 Quelques expériences sur les lames liquides minces. In *Bull. Acad. R. Belgique*, **7**, 8–18.

Quintas, M., Brandao, T. R. S., Silva, C. L. M. & Cunha, R. L. 2006 Rheology of supersaturated sucrose solutions. *J. Food Engng* **77**, 844–852.

Rayleigh, Lord 1892 On the instability of a cylinder of viscous liquid under capillary force. *Phil. Mag.* **34**(145).

Ribe, N. M. 2003 Periodic folding of viscous sheets. *Phys. Rev.* E **68**, 036305.

Ribe, N. M. 2004 Coiling of viscous jets. In *Proc. R. Soc. Lond.* A **460**, 3223–3239.

Rombauer, I. S., Becker, M. R. & Becker, E. 2006 *Joy of Cooking*, 75th edn, pp. 855–857. Scribner.

Roy, A., Mahadevan, L. & Thiffeault, J.-L. 2006 Fall and rise of a viscoelastic filament. *J. Fluid Mech.* **563**, 283–292.

Stokes, G. G. 1845 On the theories of the internal friction of fluids in motion and of the equilibrium and motion of elastic solids. *Trans. Camb. Phil. Soc.* **8**, 287–347.

Taylor, G. I. 1968 Instability of jets, threads, and sheets of viscous fluid. In *Proc. 12th Intl Congr. Appl. Mech.* pp. 382–388. Springer.

Teichman, J. & Mahadevan, L. 2003 The viscous catenary. *J. Fluid Mech.* **478**, 71–80.

Tomaszewski, W., Pieranski, P. & Geminard, J.-C. 2006 The motion of a freely falling chain tip. *Am. J. Phys.* **74**, 776–783.

Trouton, F. T. 1906 On the coefficient of viscous traction and its relation to that of viscosity. In *Proc. R. Soc Lond.* A **77**, 426–440.

Zylstra, A. B. 2007 The dynamics of viscous filaments. Unpublished analysis of the results obtained in the summer of 2006 during his participation in the Pomona College Summer Undergraduate Research Program.